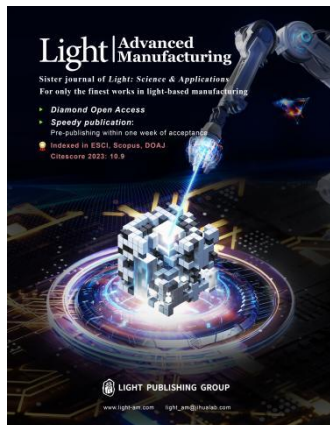


Accepted Article Preview: Published ahead of advance online publication



Dual-functional metasurfaces enabling high-efficiency holography and triple-color printing for enhanced optical security platforms

Harit Keawmuang, Dohyun Kang, Xiaotong Li, Shiqi Hu, Yeseul Kim, Minsu Jeong, Chanbeom Jeon, Peng Tang, Trevon Badloe and Junsuk Rho

Cite this article as: Harit Keawmuang, Dohyun Kang, Xiaotong Li, Shiqi Hu, Yeseul Kim, Minsu Jeong, Chanbeom Jeon, Peng Tang, Trevon Badloe and Junsuk Rho. Dual-functional metasurfaces enabling high-efficiency holography and triple-color printing for enhanced optical security platforms. *Light: Advanced Manufacturing* accepted article preview article preview 25 January, 2026; doi: 10.37188/lam.2026.022

This is a PDF file of an unedited peer-reviewed manuscript that has been accepted for publication. LAM are providing this early version of the manuscript as a service to our customers. The manuscript will undergo copyediting, typesetting and a proof review before it is published in its final form. Please note that during the production process errors may be discovered which could affect the content, and all legal disclaimers apply.

Received 10 July 2025; revised 18 December 2025; accepted 05 January;
Accepted article preview online 25 January 2026

1 **Dual-functional metasurfaces enabling high-efficiency**
2 **holography and triple-color printing for enhanced**
3 **optical security platforms**

4 **Harit Keawmuang^{1,†}, Dohyun Kang^{1,†}, Xiaotong Li^{1,†}, Shiqi Hu^{1,2}, Yeseul Kim¹,**
5 **Minsu Jeong¹, Chanbeom Jeon³, Peng Tang¹, Trevon Badloe^{4,5,*}, and Junsuk**
6 **Rho^{1,3,6,7,**}**

7 ¹ Department of Mechanical Engineering, Pohang University of Science and
8 Technology (POSTECH), Pohang 37673, Republic of Korea

9 ² Platform for Real-world Innovation in Smart Manufacturing and AI, Korea
10 Advanced Institute of Science and Technology (KAIST), Daejeon 34141, Republic of
11 Korea

12 ³ Department of Chemical Engineering, Pohang University of Science and
13 Technology (POSTECH), Pohang 37673, Republic of Korea

14 ⁴ Department of Electronics and Information Engineering, Korea University, Sejong
15 30019, Republic of Korea

16 ⁵ Division of Smart Energy Convergence Engineering, Korea University, Sejong
17 30019, Republic of Korea

18 ⁶ Department of Electrical Engineering, Pohang University of Science and
19 Technology (POSTECH), Pohang 37673, Republic of Korea

20 ⁷ POSCO-POSTECH-RIST Convergence Research Center for Flat Optics and
21 Metaphotonics, Pohang 37673, Republic of Korea

22 [†]These authors contributed equally to this work.

23 * trevon@korea.ac.kr

24 ** jsrho@postech.ac.kr

25

26

27

28

29

Abstract

Metasurfaces, flat optical devices built from nanoscale structures, offer powerful and precise control over light. They have enabled applications such as structural color printing by manipulating spectral responses and holography through precise phase control. Integrating these functions into a single metasurface has gained interest for compact multifunctional platforms. However, most existing dual-mode designs suffer from low hologram efficiency, limiting their practical applications in multifunctional optical systems. Here, we present dual-functional metasurfaces that simultaneously enable three-color structural printing under white light illumination and high-efficiency holography under coherent light. Our design employs three distinct meta-atoms, composed of single and double nanorods, to achieve independent spectral and phase modulations. The metasurfaces produce three distinct reflective colors of green, brown, and magenta and achieve numerical conversion efficiency up to 90% at the 640 nm wavelength. The fabricated devices successfully display desired structural colors under white light and reconstruct holographic images with high efficiency under coherent illumination. The devices also demonstrate broadband performance for holography across the visible spectrum. These results confirm the effectiveness of our design in achieving independent and efficient control of color and holography within a single metasurface. This multifunctional capability offers strong potential for applications in anti-counterfeiting and compact optical data storage.

Keywords: Metasurfaces, Dual-functional, Color printing, Holography, Broadband

51

52

53

54 Introduction

55 In the field of nanophotonics¹⁻³, metasurfaces, consisting of arrays of
56 subwavelength structures known as meta-atoms, have been extensively researched for
57 their revolutionary ability to precisely manipulate wavefronts and control the
58 properties of light such as amplitude, phase, orbital angular momentum, and
59 polarization⁴⁻¹². These metasurfaces have demonstrated significant potential to enable
60 a wide range of practical applications, including metalenses¹³⁻¹⁶, beam-steering^{17, 18},
61 cloaking devices^{19, 20}, solid-state light detection and ranging (LiDAR) system^{21, 22}, and
62 optical encryption devices²³⁻²⁵.

63 One particularly exciting application of metasurfaces is meta-holography. By
64 accurately controlling the spatial amplitude and phase of light, metasurfaces can be
65 designed to reconstruct holographic images, surpassing bulky optical devices such as
66 spatial light modulators with their compact and efficient design²⁶⁻²⁸. For instance, Kim
67 et al.²⁹ present meta-holograms based on a titanium dioxide
68 nanoparticle-embedded-resin, achieving a high hologram efficiency of 82%. Various
69 advanced directions in meta-holography have been explored, for example, vectorial
70 holography based on spin-orbit locking, enabling multi-channel holographic image
71 reconstruction³⁰, and real-momentum dual-functional devices based on topological
72 photonic crystals that exploit engineered disorder to encode real-space holographic
73 images while simultaneously preserving momentum-space vortex beams³¹. Moreover,
74 Asad et al.³² demonstrate a wide-angled chiral metasurface capable of spin- and
75 wavelength-multiplexed holography in the ultraviolet and visible region, achieving a
76 maximum hologram efficiency of 70% in the ultraviolet and 50% in the visible range.
77 However, most meta-holograms based solely on phase modulation face limitations
78 under typical lighting conditions. They often produce trivial reflective images or
79 display featureless, random patterns due to their lack of control over spectral
80 responses^{29, 33, 34}.

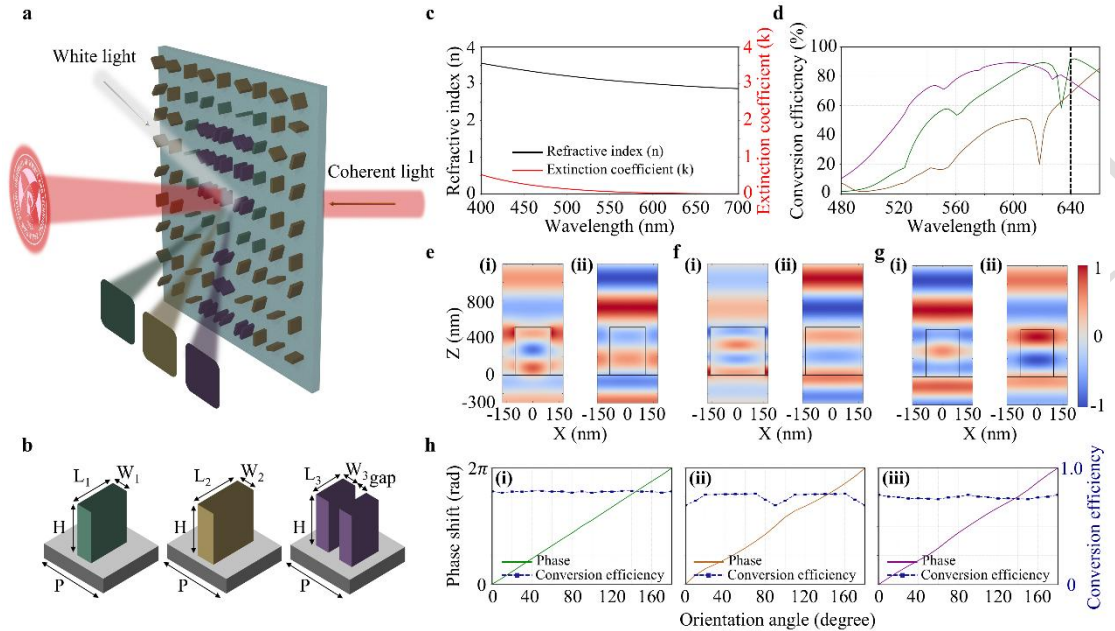
81 Another notable application of metasurfaces is color printing, where spectral
82 responses of metasurfaces are manipulated to generate high-resolution color displays³⁵.
83 ³⁶. Significant progress has been achieved in metasurfaces-based color printing
84 including polarization-multiplexed color printing³⁷, dynamic color display³⁸, and
85 polarization-encoded color image³⁹. For instance, Badloe et al.⁴⁰ demonstrate
86 electrically tunable structural color prints by integrating Mie-resonant metasurfaces
87 with liquid crystal modulation, enabling photorealistic color gradients and dark blacks
88 for dynamic reflective display and security applications. However, due to the absence
89 of encoded phase information, most color-printing metasurfaces are incapable of
90 reconstructing holographic images.

91 Some recent works, however, have addressed this limitation by simultaneously
92 controlling both phase and spectral responses, enabling metasurfaces to function
93 dually in color printing and holography⁴¹⁻⁴⁶. By integrating the dual functionalities of
94 holography and structural color prints, metasurfaces can achieve advanced optical
95 devices capable of encoding a significantly greater amount of information and
96 providing stronger encryption for security measures into a single device compared to
97 conventional methods. For instances, Yoon et al.⁴³ introduce crypto display
98 metasurfaces capable of generating reflective color printing under white light
99 illumination while reconstructing holographic image when illuminated with coherent
100 light. Their devices display two reflective colors along with a holographic image;
101 however, the hologram reconstruction efficiency is limited to around 10%, and does
102 not exhibit broadband operation. Similarly, another study⁴⁷ demonstrates metasurfaces
103 capable of displaying three reflective colors, but with hologram efficiency below 5%,
104 further restricting practical applications. Moreover, Wei et al.⁴⁴ propose a transmissive
105 metasurface design that displays two distinct color prints along with two holographic
106 images. Yet, this approach also suffers from relatively low conversion efficiency,
107 limiting the effectiveness of the holographic output. While a few studies^{48, 49} have
108 demonstrated single-cell metasurfaces that combine color printing and holography,
109 they typically exhibit hologram efficiency below 10%, which remains a major

110 limitation for real-world implementation. Furthermore, Khaleghi et al.⁵⁰ propose a
111 transmissive hybrid plasmonic–dielectric metasurface that combines color printing
112 and holography, but the two functions are implemented in different material layers,
113 and the study is limited to simulations without experimental realization.

114 Here, we propose dual-functional metasurfaces that integrate color printing mode
115 and holography mode multiplexing on a single layer dielectric metasurface that
116 provides three distinct printing colors, which are green, brown, and magenta as well
117 as achieves high conversion efficiency to maximize holographic image quality. By
118 using three distinct meta-atoms based on Pancharatnam-Berry (PB) or so-called
119 geometric phase, we can simultaneously modulate both reflectance spectra under
120 white light illumination and spatial phase distribution of single wavelength coherent
121 light. The schematic representation of the dual-functional metasurfaces is illustrated
122 in Fig. 1a. We employ single and double nanorods as our meta-atoms, which spectral
123 response and conversion efficiency can be tuned by adjusting the size of the nanorods,
124 while phase distribution is controlled by varying their orientation. The nanorods are
125 designed to achieve high conversion efficiency at the target wavelength of 640 nm,
126 while also exhibiting unique reflectance spectra for a variety of reflective colors.
127 Moreover, numerical simulations show that among the designed meta-atoms, the
128 highest-performing one achieves a conversion efficiency of up to 90% at the target
129 wavelength. The fabricated samples successfully demonstrate three distinct reflective
130 colors under white light and high-efficiency holography under coherent light. The
131 designed metasurfaces also exhibit broadband characteristics for holography,
132 operating across a broad range of the visible spectrum. By enabling three reflective
133 colors with broadband holographic capability, this dual-functional metasurface
134 enhances information capacity and offers greater flexibility for data encryption.
135 Moreover, high hologram efficiency enables bright, high-contrast image
136 reconstruction even under low-intensity illumination, reducing power requirements
137 and enhancing usability under limited or low-light conditions without sacrificing
138 image quality. These advantages make the proposed metasurfaces a promising

139 platform for applications requiring advanced data security, such as anti-counterfeiting,
 140 authentication, and encrypted data storage.



141

142 **Fig. 1 Design and optical performance of the dual-functional metasurface.** **a** Schematic
 143 illustration of the metasurface functionality, showing reflective color generation under white
 144 light and holographic image reconstruction under coherent light illumination. **b** Structural
 145 designs of the three meta-atoms, meta-atoms 1, 2, and 3, corresponding to green, brown, and
 146 magenta reflective colors, respectively. **c** Refractive index (n , black) and extinction
 147 coefficient (k , red) of hydrogenated amorphous silicon (a-Si:H). **d** Conversion efficiency of
 148 meta-atom 1 (green), meta-atom 2 (brown), and meta-atom 3 (magenta) across the visible
 149 wavelength range. **e–g** Electric field distributions in the xz -plane for meta-atoms 1, 2, and 3,
 150 respectively, under (i) x-polarized and (ii) y-polarized illumination. **h** Simulated phase shift
 151 (solid line) and conversion efficiency (dashed line) as functions of the meta-atom orientation
 152 angle for meta-atoms (i) 1, (ii) 2, and (iii) 3.

153 Results and discussions

154 In order to achieve a dual-functional capability, every unit cell of the metasurface
 155 must satisfy two key requirements. First, their conversion efficiency must be high at
 156 the target wavelength (640 nm) to maximize the performance of the holography mode.
 157 Second, their spectral responses must be sufficiently distinct to produce different
 158 reflective colors. Since the total energy is conserved between reflection and
 159 transmission, there naturally exists a trade-off in their efficiencies. In our design, we

160 aim to balance these two aspects by ensuring sufficiently high reflection contrast for
161 color printing while maintaining high conversion efficiency in the transmission
162 channel to support holography. To meet these conditions, anisotropic nanostructures
163 are employed with circularly polarized illumination, enabling PB phase modulation
164 while maintaining identical spectral responses. Phase modulation can be achieved by
165 adjusting the azimuthal angles of the meta-atoms, while their spectral responses can
166 be independently tuned by altering their size, ensuring no mutual interference. We
167 utilize both single and double nanorod designs as our meta-atoms to expand the range
168 of spectral responses, thereby offering a wider selection of colors. Additionally, the
169 single nanorod design allows higher fabrication accuracy by accommodating larger
170 dimensions for the structure.

171 This work utilizes three types of meta-atoms, referred to as meta-atom 1,
172 meta-atom 2, and meta-atom 3, corresponding to the reflective colors green, brown,
173 and magenta, respectively, as illustrated in Fig. 1b. By adjusting key geometric
174 parameters such as periodicity (P), height (H), length (L), and width (W) of the
175 nanostructures, we optimize their design to achieve high conversion efficiency at 640
176 nm wavelength and distinct reflectance spectra across all meta-atoms. The optical
177 responses are obtained by using rigorous coupled wave analysis (RCWA) simulations.
178 Meta-atoms 1 and 2 are based on a single nanorod structure, while meta-atom 3
179 adopts a double nanorod configuration to realize the desired optical response. Every
180 meta-atom has the same P of 350 nm and H of 515 nm, while other structural
181 parameters are different with $L_1 = 205$ nm, $W_1 = 95$ nm, $L_2 = 315$ nm, $W_2 = 100$ nm,
182 $L_3 = 190$ nm, and $W_3 = 80$ nm with a 100 nm gap between the rods. Supplementary
183 Note 1 presents conversion efficiency maps at the target wavelength as a function of L
184 and W . The effect of gap size on the spectral response and conversion efficiency is
185 further investigated in Supplementary Note 2. The values of P and H are selected after
186 sweeping a range of parameters to identify a configuration that performs well for both
187 single and double nanorod. The meta-atoms are made of hydrogenated amorphous
188 silicon (a-Si:H) deposited on a glass substrate. While normal amorphous silicon

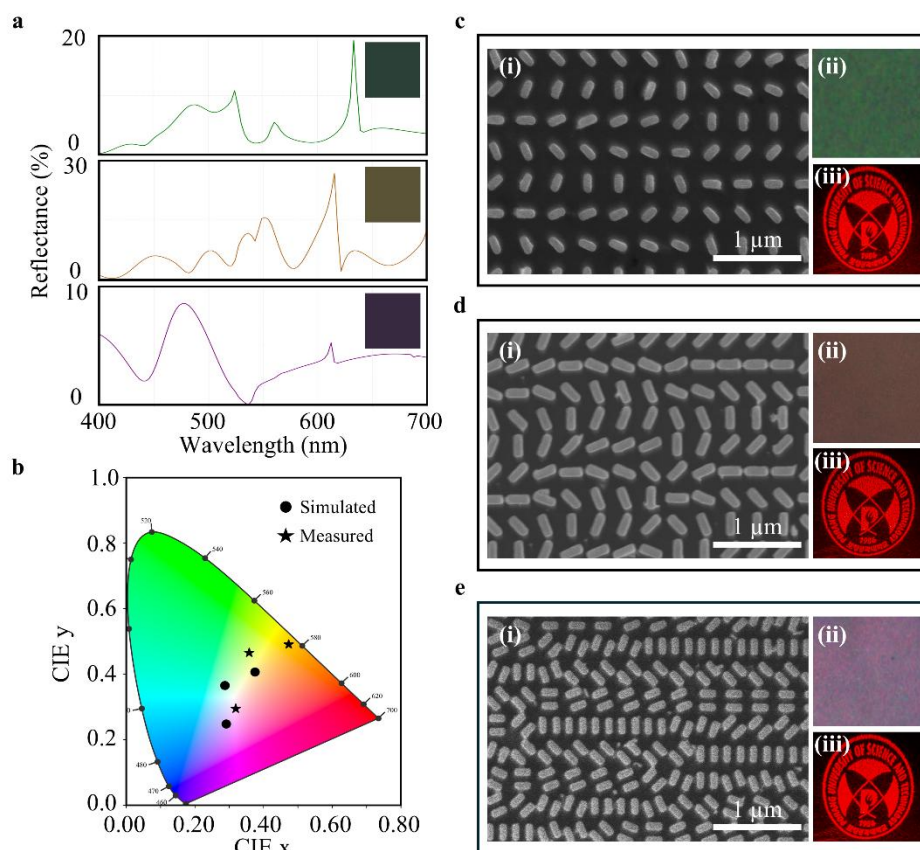
189 exhibits high refractive index in the visible wavelength range, its strong optical loss
190 limits diffraction efficiency⁴³. In contrast, a-Si:H incorporates hydrogen to reduce the
191 defect density typically found in amorphous silicon, thereby enhancing its optical
192 properties for visible metasurfaces by lowering optical losses at visible wavelengths⁵¹.
193 The optical properties of a-Si:H used in this study are shown in Fig. 1c. The
194 conversion efficiency represents how effectively the incoming right-handed circularly
195 polarized (RCP) light is converted into outgoing left-handed circularly polarized (LCP)
196 light. The outgoing LCP component carries the desired phase information encoded on
197 the metasurface, while the transmitted RCP does not. Therefore, the conversion
198 efficiency is directly linked to the hologram efficiency of the metasurface. Fig. 1d
199 presents the simulated conversion efficiency of meta-atoms 1, 2, and 3 across the
200 visible wavelength range from 480 to 660 nm. A vertical dashed line at 640 nm marks
201 the target wavelength. All three designs exhibit increasing conversion efficiency as
202 the wavelength approaches 640 nm. Meta-atoms 1 and 2 reach conversion efficiency
203 of 91% and 68% at 640 nm, respectively. Meta-atom 3 achieves 77% at the target
204 wavelength and maintains a broader high-efficiency bandwidth across the visible
205 spectrum. These results confirm that all three meta-atoms are well-optimized for
206 strong polarization conversion at the operating wavelength.

207 Moreover, to demonstrate that all the meta-atoms behave as half-wave plates,
208 effectively converting incident RCP light into outgoing LCP, we confirm their
209 functionality through finite-difference time-domain (FDTD) simulations at the target
210 wavelength of 640 nm. These simulations evaluate the electric field (E-field)
211 distribution in the xz-plane under both (i) x-polarized and (ii) y-polarized incident
212 light for each meta-atom, as shown in Fig. 1e–g, corresponding to meta-atoms 1, 2,
213 and 3, respectively. The results show a consistent π phase difference between the two
214 polarization states across all designs, confirming that the meta-atoms effectively
215 function as half-wave plates. Moreover, to verify the phase modulation behavior of
216 the meta-atoms based on PB phase principle, we perform RCWA simulations to
217 calculate the phase shift and conversion efficiency as functions of the meta-atom

218 orientation angle at the operating wavelength of 640 nm. As presented in Fig. 1h, all
219 three meta-atom designs (i) 1, (ii) 2, and (iii) 3 exhibit a continuous phase shift
220 covering the full $0-2\pi$ range as their orientation angle varies from 0° to 180° .
221 Importantly, the conversion efficiency remains consistently high across all angles,
222 indicating that phase modulation is governed solely by the geometric phase term $\Phi =$
223 $2\sigma\varphi$, where φ is the in-plane rotation angle and σ denotes the helicity of incident
224 circularly polarized light. These results confirm that the meta-atoms provide
225 independent phase control while maintaining high polarization conversion efficiency,
226 which is essential for integrating both holography and color printing functionalities
227 into a single metasurface.

228 To achieve three distinct color outputs under white light illumination, the
229 meta-atoms are designed to exhibit unique reflectance spectra across the visible range.
230 These spectral responses are calculated using RCWA, and the corresponding
231 structural colors are obtained by performing spectral-to-color conversion over the
232 visible wavelength range of 400–700 nm, based on the simulated reflectance spectra
233 and the CIE 1931 standard observer functions. The spectra-to-color conversion
234 routine is detailed in Supplementary Note 3. Again, to meet the dual requirements of
235 high conversion efficiency at 640 nm and distinct color generation, we employ two
236 types of nanorod configurations. This strategy expands the accessible color space,
237 allowing for more flexible and effective meta-atom selection. The simulated color
238 space resulting from these configurations is presented in Supplementary Note 4. Fig.
239 2a presents the simulated reflectance spectra of the selected meta-atoms 1, 2, and 3,
240 along with their corresponding colors. Meta-atoms 1, 2, and 3 correspond to green,
241 brown, and magenta, respectively. These colors are specifically adopted because their
242 spectral responses are sufficiently distinct, ensuring clearly distinguishable reflective
243 colors, while also maintaining high conversion efficiency at 640 nm, which is critical
244 for the holography mode. We note that although green, brown, and magenta are
245 demonstrated here, the color scheme can be extended to primary RGB (red, green, and
246 blue) or other choices by tailoring the nanostructure geometries or employing

247 alternative material platforms^{47, 48}. Then, we fabricate each metasurface based on the
 248 corresponding meta-atom designs. After fabrication of the metasurfaces, we measure
 249 the reflectance spectra of each sample using Fourier-transform infrared (FT-IR)
 250 spectroscopy. The measured spectra are then converted into colors using the same
 251 spectral-to-color conversion procedure. As shown in Fig. 2b, both the simulated
 252 (circles) and experimentally measured (stars) chromaticity coordinates are plotted on
 253 the CIE 1931 diagram. The differences between the simulated and measured colors
 254 are primarily attributed to fabrication-induced variations in meta-atom structural
 255 parameters. Process fluctuations during electron beam lithography, development, and
 256 etching lead to slight inconsistencies in meta-atom dimensions, even within the same
 257 metasurface.



258

259 **Fig. 2 a** Simulated reflectance spectra of meta-atom 1 (top), meta-atom 2 (middle), and
 260 meta-atom 3 (bottom). The insets show the resulting structural colors under white light
 261 illumination, green, brown, and magenta, respectively. **b** CIE 1931 chromaticity diagram
 262 showing the simulated (circles) and measured (stars) color coordinates for each meta-atom.
 263 **c–e** (i) Scanning electron microscope (SEM) images of the fabricated metasurfaces; (ii)

264 Corresponding optical microscope images showing the structural colors under white light
265 illumination; and (iii) Holographic image reconstructions of the university logo under red
266 laser illumination. The scale bars in the SEM images represent 1 μm .

267 For the holography mode, we use computer-generated phase-only Fourier
268 holography to encode the holographic image to the metasurfaces. We design the target
269 holography image of 1200×1200 pixels of our university logo and encode it using
270 the Gerchberg-Saxton (GS) algorithm (see Supplementary Note 5). The GS algorithm
271 iterates for a thousand iterations to retrieve the simulated holography image. Then, the
272 continuous phase distribution obtained from the algorithm is transformed into a
273 discrete phase distribution by dividing the 0 to 2π phase range into eight equal steps.
274 Next, the meta-atoms are oriented according to the obtained phase distribution. We
275 note that the orientation of the meta-atoms does not have any effect on their spectral
276 responses. Moreover, to mitigate the impact of the zeroth-order beam (ZOB), we
277 implement an off-axis configuration for the designed target holographic image. The
278 ZOB occurs because the conversion efficiency of metasurface is not perfect, meaning
279 that part of incident light remains in the co-polarized state and propagates as
280 undiffracted light, which appears as a bright spot at the center of the Fourier plane. If
281 the hologram's image pixel matches that of the metasurface, the ZOB would appear at
282 the center of the generated holographic image, compromising the image fidelity. The
283 illustration of this overlap is presented in Fig. S5b, Supplementary Note 6. To address
284 this, we reduce the size of the target holographic image and shift it upward,
285 effectively avoiding interference from the ZOB (Fig. S5d, Supplementary Note 6).

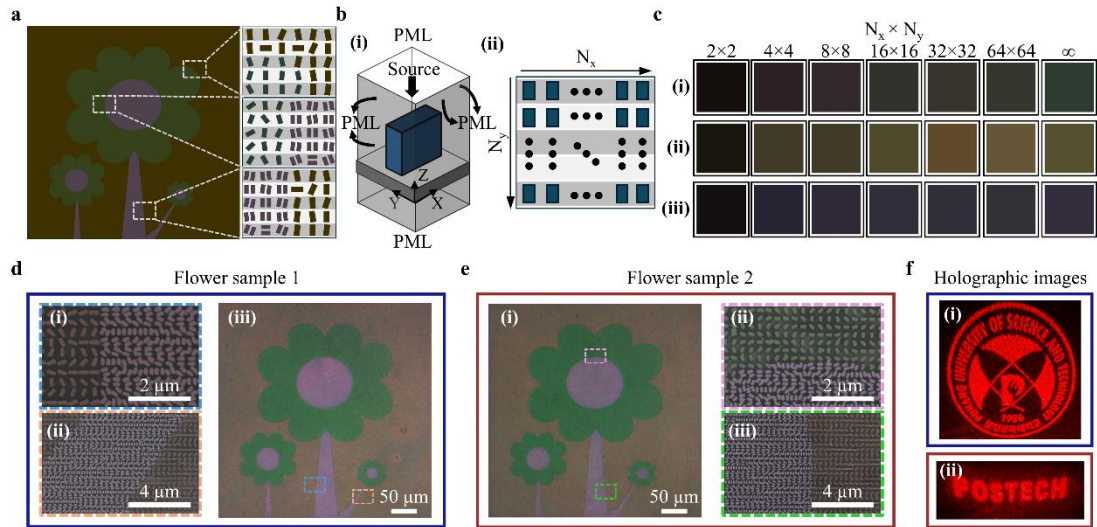
286 Fig. 2c–e showcase the performance of the fabricated dual-mode metasurfaces
287 corresponding to the three meta-atom designs. The size of metasurfaces is 420×420
288 μm , containing 1200×1200 pixels for all the samples. Fig. 2c–e correspond to three
289 distinct metasurface designs, with each panel displaying (i) a scanning electron
290 microscope (SEM) image, (ii) an optical microscope image captured under
291 unpolarized white light illumination from a light-emitting diode (LED) representing
292 the color printing mode, and (iii) a holographic image projected under coherent light

illumination representing the holography functionality. To obtain the microscopic images, a charge-coupled device (CCD) camera is connected to the eyepiece of the optical microscope. These results show that, despite minor fabrication imperfections, the observed structural colors remain in good agreement with the simulated results. For the holography demonstration, we employ a supercontinuum laser source spanning 400–2000 nm, combined with a tunable bandpass filter to select specific wavelengths. The metasurfaces are illuminated at 640 nm to reconstruct the encoded holographic image. The generated holographic images are captured as photographs of the projections on a screen. See Supplementary Note 7 for a schematic of the optical experiment set up used to reconstruct a holographic image. It is worth noting that additional polarization optics, such as a second set of quarter-wave plate and linear polarizer, can be employed after the light passes through the metasurface to suppress the co-polarized zero-order component, as demonstrated in previous work³², where both the co- and cross-polarized beams propagate along the same optical axis. However, such a configuration increases optical complexity, making the system bulkier, harder to align, and requiring simultaneous control of both the input and output polarization components to maintain proper polarization filtering. It also poses challenges for integration and miniaturization. In contrast, our off-axis design diffracts the cross-polarized holographic beam upward at an oblique angle, resulting in spatial separation from the zero-order beam. This eliminates the need for extra polarization analyzers, enabling a simpler and more efficient optical setup. To further investigate the effect of incident polarization on hologram reconstruction of our metasurfaces, we conduct additional hologram experiments using RCP, LCP, and LP illumination at the same wavelength. As presented in Fig. S7, the metasurface reconstructs a high-quality holographic image under the designed RCP illumination. When illuminated with LCP light, a similar holographic image appears at a centrosymmetric position due to the geometric phase response of the metasurface. Under LP illumination, which can be decomposed into a superposition of RCP and LCP components, both holographic images appear simultaneously on the screen as

322 symmetric duplicates. These results show that our metasurfaces produce high-quality
323 holographic images under all three polarization states. Importantly, despite the
324 differences in structural color and meta-atom dimensions across the three
325 metasurfaces, the reconstructed holographic images remain nearly identical. This
326 highlights the independent operation of the two functional modes of our devices.

327 To demonstrate the enhanced information capacity and cryptographic flexibility
328 of our platform, we integrate all three meta-atom designs onto a single metasurface.
329 We design a target image of flowers composed of three distinct colors, as shown in
330 Fig. 3a, where the leaves are assigned to appear green, the background is designated
331 as brown, and the flower center and stem (body) are rendered in magenta. These green,
332 brown, and magenta colors correspond to the measured structural colors of
333 meta-atoms 1, 2, and 3, respectively. To realize this image, we assign each pixel a
334 meta-atom corresponding to its target color. The zoom-in regions highlight areas
335 where different meta-atoms are spatially distributed according to the target colors. For
336 example, the green leaf region is composed of meta-atom 1, while the adjacent
337 magenta region at the center of the flower is realized by meta-atom 3. Similarly, the
338 stem (body) and the adjacent background are assigned with meta-atoms 3 and 2,
339 respectively. This spatial distribution of multiple meta-atoms demonstrates the ability
340 to display multiple colors within a single metasurface. The simulated reflectance
341 spectra shown in Fig. 2a assume an ideal metasurface modeled as an infinite array
342 using periodic boundary conditions. However, in practice, finite-sized metasurfaces
343 exhibit slight deviations in reflectance spectra, especially when multiple types of
344 meta-atoms are integrated onto the same surface, which limits the array size of each
345 design and leads to subtle variations in the resulting structural colors. To investigate
346 this effect, we perform FDTD simulations by applying perfectly matched layer (PML)
347 boundary conditions along the X and Y axes instead of periodic boundaries. The
348 Z-direction boundaries are also set to PML to capture the reflected fields, with the
349 light source incident along the Z axis (Fig. 3b(i)). Then, we simulate finite arrays of
350 meta-atoms, represented by dimensions $N_x \times N_y$, where N_x and N_y denote the numbers

351 of meta-atoms along x- and y- directions along metasurface, respectively, to
352 investigate how array size influences the resulting structural colors (Fig. 3b(ii)).
353 Specifically, we consider square arrays with $N_x = N_y = 2, 4, 8, 16, 32, 64$, and infinity
354 to evaluate the effect of increasing metasurface size. Fig. 3c(i–iii) presents the
355 structural colors resulting from different array sizes ($N_x \times N_y$) for meta-atoms 1, 2, and
356 3, respectively. We note that the colors obtained under infinite periodic boundary
357 conditions in the FDTD simulations show good agreement with the results from
358 RCWA simulations, validating the consistency between the two computational
359 approaches. Moreover, the structural colors are observed to gradually converge as the
360 number of meta-atoms increases for all three designs. Notably, meta-atoms 2 and 3
361 begin to exhibit distinguishable colors even in relatively small arrays of 4×4 .
362 Meta-atom 2 produces a recognizable brown hue from 4×4 onward and continues to
363 display vivid colors throughout the simulation as the array size increases despite
364 minor variations in hue. Similarly, meta-atom 3 begins to display a dark magenta
365 color at 4×4 , with a slight bluish tone. In contrast, meta-atom 1, which is designed to
366 produce green, requires a larger array size for accurate color formation, however, it
367 starts to show dark green color at the 64×64 arrays. We note that when different
368 types of meta-atoms are integrated in close proximity, the perceived structural colors
369 can be affected by the relative array size ratio of each meta-atom type, as
370 demonstrated in the previous study⁴⁰. However, in this work, we use sufficiently large
371 arrays of each meta-atom type, so the perceived colors remain unchanged.

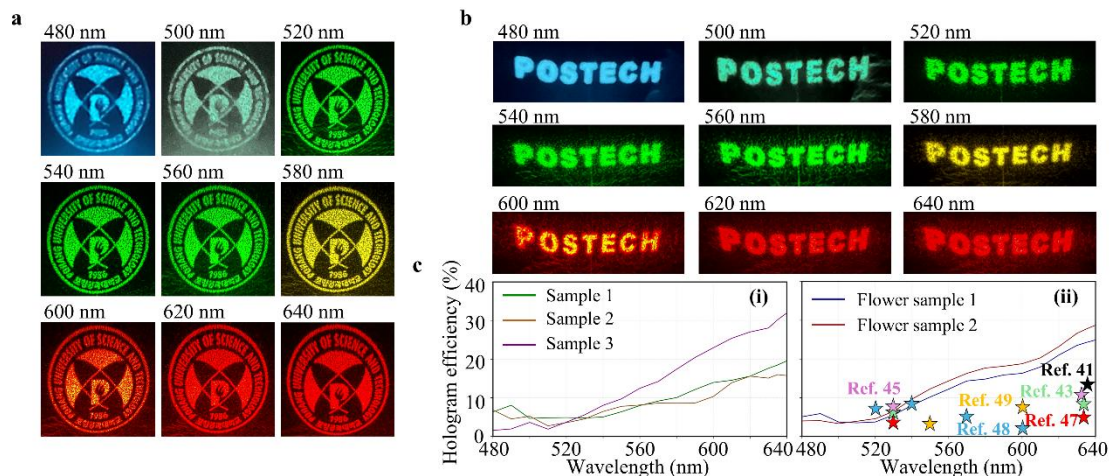


372

373 **Fig. 3** **a** Target flower image composed of three colors based on the measured colors of the
 374 meta-atoms: green for leaves, brown for background, and magenta for the flower center and
 375 stem (body). The right panels show a zoom-in view of the pixel-level meta-atom assignments
 376 in the different regions. **b** FDTD simulation setup for finite metasurface arrays: (i) 3D
 377 schematic showing perfectly matched layer (PML) boundary conditions in all directions and a
 378 normally incident light source along the $-Z$ axis; (ii) Schematic of finite arrays with varying
 379 numbers of meta-atoms $N_x \times N_y$. **c** Simulated structural colors for different array sizes ranging
 380 from 2×2 to infinity, with rows (i)-(iii) corresponding to meta-atoms 1, 2, and 3, respectively.
 381 **d** Optical and SEM characterization of Flower Sample 1: (i, ii) SEM images of different
 382 selected regions showing spatially assigned meta-atoms; (iii) Optical microscope image of the
 383 printed color pattern. **e** Optical and SEM characterization of Flower Sample 2: (i) Optical
 384 microscope image of the printed color pattern; (ii, iii) SEM images of different selected
 385 regions showing spatially assigned meta-atoms. **f** Holographic images reconstructed under
 386 640 nm coherent illumination: (i) POSTECH university logo from Flower Sample 1, and (ii)
 387 “POSTECH” text from Flower Sample 2. Scale bars: $2 \mu\text{m}$ and $4 \mu\text{m}$ for SEM images, $50 \mu\text{m}$
 388 for optical microscope images.

389 We fabricate two flower samples by assigning meta-atoms to each pixel
 390 according to the target color image. Both samples are designed to produce the same
 391 structural color print, while their holographic targets are encoded differently to
 392 demonstrate the independent control of the dual modes. Fig. 3d and 3e highlight the
 393 color printing capabilities of the designed metasurfaces, with zoomed-in SEM images
 394 from different regions revealing the spatial distribution of distinct meta-atoms
 395 corresponding to the target colors. For instance, Fig. 3d(ii) illustrates the spatial
 396 transition between two different meta-atom designs, providing a zoomed-in SEM
 397 view of the lower stem region, showing the transition between meta-atom 2 (brown)

398 and meta-atom 3 (magenta). The structural colors observed in the optical images
 399 match well with the designed target colors in each part of the flower. Moreover, the
 400 overall flower patterns in both samples appear nearly identical in color and layout,
 401 despite being encoded with different holographic phase profiles. For the holography,
 402 Flower Sample 1 is encoded with the POSTECH university logo, while Flower
 403 Sample 2 is encoded with the text “POSTECH”. When illuminated with a
 404 single-wavelength coherent light at 640 nm using the same supercontinuum laser, the
 405 resulting holographic images projected onto a screen are captured and shown in Fig.
 406 3f: (i) corresponds to Flower Sample 1, and (ii) to Flower Sample 2. These results
 407 demonstrate that identical structural color prints can be combined with distinct
 408 holographic images, highlighting the dual-mode functionality of the metasurface
 409 platform.



410

411 **Fig. 4 a** Broadband holographic images reconstructed from Flower Sample 1, illuminated
 412 with a supercontinuum laser tuned from 480 nm to 640 nm in 20 nm steps. **b** Broadband
 413 holographic images reconstructed from Flower Sample 2 under identical illumination
 414 conditions. **c** Measured hologram efficiency across the visible spectrum. (i) Hologram
 415 efficiency of individual meta-atom samples, samples 1, 2, and 3, each corresponding to
 416 meta-atom 1, 2, and 3, respectively. (ii) Hologram efficiency of Flower Sample 1 and Flower
 417 Sample 2 plotted alongside representative data from recent dual-mode metasurface studies for
 418 comparison.

419

420

To demonstrate the broadband characteristics of our metasurfaces, we perform
 hologram experiments for Flower Sample 1 and Flower Sample 2 across the visible

421 spectrum using the same supercontinuum laser source. The output wavelength was
422 tuned from 480 nm to 640 nm in 20 nm increments using a tunable bandpass filter.
423 The resulting holographic images are shown in Fig. 4a for Flower Sample 1 and in Fig.
424 4b for Flower Sample 2. These results confirm the broadband performance of both
425 metasurfaces across the visible range. We also measure the hologram efficiency to
426 investigate the performance differences among the various metasurface samples.
427 Hologram efficiency is defined as the ratio of the optical power contained in the
428 reconstructed holographic image to the total incident optical power. Fig. 4c(i) shows
429 the measured hologram efficiency of individual metasurface samples, samples 1, 2
430 and 3, each composed of a uniform array of meta-atoms 1, 2, and 3, respectively.
431 Hologram efficiency of all samples increases with wavelength, gradually rise across
432 the visible range, with the highest efficiency reaching up to over 30% at the target
433 wavelength (640 nm). In PB phase metasurfaces, this efficiency is strongly correlated
434 with the meta-atom conversion efficiency, as the holographic image is formed by the
435 transmitted cross-polarized light. The measured efficiency trends for each sample
436 closely follow the corresponding meta-atom conversion efficiency curves, all showing
437 a gradual increase with wavelength. Notably, the difference between the simulated
438 and measured efficiencies may arise from residual zeroth-order power. Incomplete
439 polarization conversion leaves a co-polarized component that propagates undiffracted
440 into the zeroth order, which does not carry the designed phase and therefore reduces
441 the fraction of incident power directed into the holographic image. In addition,
442 fabrication imperfections, alignment errors, and wavelength fluctuations can further
443 enhance the relative intensity of the zeroth-order component. To minimize this effect,
444 one can enhance the conversion efficiency of the meta-atom by carefully optimizing
445 the nanostructure geometry and employing improved material design²⁹. Tighter
446 fabrication tolerances can also ensure that the fabricated meta-atoms perform closer to
447 the ideal design, thereby further suppressing residual zeroth-order power. In addition,
448 we benchmark our performance against recent works on dual-functional metasurfaces,
449 which are indicated in Fig. 4c(ii) as colored star markers. We note that a single

450 reference may correspond to multiple markers, each indicating hologram efficiency at
451 a specific wavelength. The results demonstrate that our samples exhibit competitive or
452 superior broadband performance compared to other works, particularly near the target
453 wavelength, further validating the effectiveness of our designs.

454 **Conclusion**

455 In conclusion, we propose dual-functional metasurfaces that simultaneously
456 produce three vivid structural color prints under white light illumination and enable
457 high efficiency holography under single wavelength coherent light within a single
458 optical platform. The metasurfaces consist of three types of meta-atoms based on
459 single and double nanorods. Each meta-atom is designed to exhibit a distinct spectral
460 response corresponding to a specific color while maintaining high conversion
461 efficiency for holographic functionality. Meta-atom 1, 2, and 3 generate green, brown,
462 and magenta colors, respectively, and each demonstrate high conversion efficiency,
463 reaching up to 90% at the target wavelength of 640 nm. GS algorithm is used to
464 encode phase information for holography to assign the orientation of each meta-atom.
465 Then, we demonstrate spatial integration of these meta-atoms by fabricating a
466 metasurface that displays a multicolor pattern, along with an encoded holographic
467 image. The color prints correspond well to the designed colors, while the holograms
468 vary according to the encoded phase design, highlighting the independence of the two
469 functionalities. The devices also show broadband performance, reconstructing
470 holograms across the visible spectrum. Notably, we compare hologram efficiency of
471 our dual-functional devices with recent works, showing that our designs achieve
472 comparable or superior broadband performance, particularly near the target
473 wavelength. Importantly, higher hologram efficiency contributes to better image
474 contrast and brightness while reducing the required source intensity and overall power
475 consumption. This makes the devices more energy-efficient and practical for
476 real-world deployment. This work presents a compact and versatile platform that
477 combines visual aesthetics with information encoding, offering strong potential for

478 advanced applications in data encryption, secure authentication, anti-counterfeiting,
479 and multifunctional display technologies. Future work could explore the use of
480 inverse design strategies based on deep learning⁵² or advanced optimization methods⁸
481 to enable the automated discovery of meta-atom configurations capable of generating
482 on-demand colors with high accuracy.

483 **Materials and Methods**

484 **Experimental setup**

485 Reflectance spectra of the fabricated metasurfaces are measured by FT-IR, and the
486 microscopic images are captured by a CCD with a white LED. To reconstruct the
487 holographic images, we set up an optical system using a supercontinuum laser
488 (SuperK FIANIUM, NKT Photonics) as the light source. A tunable bandpass filter
489 (LLTF Contrast, NKT Photonics) is placed at the output to select the desired
490 wavelength. The beam passes through a 500 μm iris to adjust its size, followed by a
491 linear polarizer (LPVISE050-A, Thorlabs, USA) and a quarter-wave plate
492 (AQWP05M-600, Thorlabs) to generate right-handed circularly polarized (RCP) light.
493 After passing through the metasurface, the modulated light forms the holographic
494 image, which is projected onto a screen placed in the far field.

495 **Numerical simulation**

496 An in-house rigorous coupled-wave analysis (RCWA) code is used to compute the
497 spectral response and conversion efficiency of the designed meta-atoms. To evaluate
498 half-wave plate behavior and the influence of finite array size on structural colors, a
499 commercial finite-difference time-domain (FDTD) solver (Lumerical FDTD, Ansys
500 Inc.) is employed. Perfectly matched layer (PML) boundary conditions are applied
501 along all axes, with the incident light propagating along the -Z direction. Finite arrays
502 consisting of $N_x \times N_y$ meta-atoms, where $N_x \times N_y$ the number of meta-atoms along the
503 x- and y-directions, respectively, are simulated to investigate array-size dependent
504 effects on structural colors.

505 Sample fabrication

506 The metasurfaces are fabricated through a conventional electron-beam lithography
507 process. A 515 nm thick a-Si:H film is deposited on a glass substrate using
508 plasma-enhanced chemical vapor deposition (BMR Technology, HiDep-SC). A
509 positive photoresist (ZEP-520A) is spin-coated at 5,000 rpm for 1 minute and baked
510 at 180 °C for 3 minutes. A conductive polymer (Showa Denko, Espacer 300Z) is
511 spin-coated at 2,000 rpm for 1 minute to avoid electron accumulation during exposure.
512 Then, the target pattern is exposed with electron-beam lithography (ELS-BODEN,
513 ELIONIX, acceleration voltage: 50 kV, beam current 10 nA). The exposed pattern is
514 transferred by developing with ZED-N50 at 0°C for 1 minute after removing the
515 conductive layer by dipping in DI water for 1 minute. A 50 nm thick chromium (Cr)
516 layer is deposited using electron-beam evaporation (KVT, KVE-ENS4004). The
517 unwanted Cr layer is immersed in acetone at 60 °C for 1 hour, followed by a dry etch
518 (DMS, silicon/metal hybrid etcher) with Cr as a hard mask. The remaining Cr etching
519 mask is removed by Cr etchant (CR-7).

520 Acknowledgements

521 H.K., D.K., and X.L. contributed equally to this work. This work was financially
522 supported by the POSCO-POSTECH-RIST Convergence Research Center program
523 funded by POSCO, and the National Research Foundation (NRF) grant
524 (RS-2022-NR067559) funded by the Ministry of Science and ICT (MSIT) of the
525 Korean government. H.K. acknowledges the POSCO Asia fellowship, and the Yuhan
526 Foundation *New Ilhan* fellowship. X.L. acknowledges the China Scholarship Council
527 (CSC) fellowship (202306890039). S.H. acknowledges the InnoCORE program
528 (N10250154) funded by the MSIT of the Korean government.

529 Author Contributions

530 H.K., D.K., and X.L. contributed equally to this work. J.R. conceived the idea and
531 initiated the project. H.K. designed the metasurfaces and conducted numerical

532 simulations. D.K. fabricated the devices. H.K., D.K., X.L., S.H., Y.K., M.J., C.J., and
533 P.T. conducted optical characterizations and measurements. H.K. and X.L. carried out
534 hologram experiments. All authors confirmed the final manuscript. J.R. and T.B.
535 guided the entire project.

536 **Data availability**

537 All data are available from the corresponding authors upon reasonable request.

538 **Conflict of interest**

539 The authors declare no competing interests.

540 **Supplementary information**

541 Supplementary materials are available at the online version.

542 **References**

- 543 1. González-Tudela, A. et al. Light–matter interactions in quantum
544 nanophotonic devices. *Nature Reviews Physics* **6**, 166-179 (2024).
- 545 2. So, S. et al. Deep learning enabled inverse design in nanophotonics.
546 *Nanophotonics* **9**, 1041-1057 (2020).
- 547 3. Park, J. et al. Flexible self - cleaning janus emitter for transparent radiative
548 cooling in enclosed spaces. *Small* **21**, 2501840 (2025).
- 549 4. Choi, M. et al. Realization of high-performance optical metasurfaces over a
550 large area: a review from a design perspective. *npj Nanophotonics* **1**, 31
551 (2024).
- 552 5. Yu, N. F. & Capasso, F. Flat optics with designer metasurfaces. *Nature*
553 *Materials* **13**, 139-150 (2014).
- 554 6. Jahani, S. & Jacob, Z. All-dielectric metamaterials. *Nature Nanotechnology*

- 555 **11**, 23-36 (2016).
- 556 7. Park, J. et al. Electrically tunable metasurfaces for broadband beam
557 splitting across the visible spectrum. *Advanced Optical Materials* **13**, 2403413
558 (2025).
- 559 8. Keawmuang, H. et al. Hybrid frameworks integrating deep learning and
560 optimization methods for inverse design in nanophotonics. *ACS Applied*
561 *Materials & Interfaces* **17**, 33259-33270 (2025).
- 562 9. Jung, C. et al. Metasurface-driven optically variable devices. *Chemical*
563 *Reviews* **121**, 13013-13050 (2021).
- 564 10. Kim, Y. et al. Spin-dependent phenomena of meta-optics. *ACS Photonics*
565 **12**, 16-33 (2025).
- 566 11. Tang, P. et al. Spin hall effect of light in a dichroic polarizer for
567 multifunctional edge detection. *ACS Photonics* **11**, 4170-4176 (2024).
- 568 12. Kim, Y. et al. Topological vortex transition induced by spin hall effect of
569 light for tunable humidity sensing and imaging. *Laser & Photonics Reviews* **19**,
570 e00581.
- 571 13. Moon, S. W. et al. Recent progress on ultrathin metalenses for flat optics.
572 *iScience* **23**, 101877 (2020).
- 573 14. Arbabi, A. & Faraon, A. Advances in optical metalenses. *Nature Photonics*
574 **17**, 16-25 (2023).
- 575 15. Park, J., Kim, G. & Rho, J. Advancing depth perception in spatial
576 computing with binocular metalenses. *Opto-Electronic Advances* **8**, 240267
577 (2025).
- 578 16. Li, X. T. et al. Cascaded metasurfaces enabling adaptive aberration

- 579 corrections for focus scanning. *Opto-Electronic Advances* **7**, 240085 (2024).
- 580 17. Wei, Z. Y. et al. Highly efficient beam steering with a transparent
581 metasurface. *Optics Express* **21**, 10739-10745 (2013).
- 582 18. Thureja, P. et al. Array-level inverse design of beam steering active
583 metasurfaces. *ACS Nano* **14**, 15042-15055 (2020).
- 584 19. Chu, H. C. et al. A hybrid invisibility cloak based on integration of
585 transparent metasurfaces and zero-index materials. *Light: Science &*
586 *Applications* **7**, 50 (2018).
- 587 20. Xu, H. X. et al. Polarization-insensitive 3D conformal-skin metasurface
588 cloak. *Light: Science & Applications* **10**, 75 (2021).
- 589 21. Juliano Martins, R. et al. Metasurface-enhanced light detection and
590 ranging technology. *Nature Communications* **13**, 5724 (2022).
- 591 22. Kim, I. et al. Nanophotonics for light detection and ranging technology.
592 *Nature Nanotechnology* **16**, 508-524 (2021).
- 593 23. Kim, J. et al. Photonic encryption platform via dual-band vectorial
594 metaholograms in the ultraviolet and visible. *ACS Nano* **16**, 3546-3553 (2022).
- 595 24. Zheng, P. X. et al. Metasurface-based key for computational imaging
596 encryption. *Science Advances* **7**, eabg0363 (2021).
- 597 25. Zhu, L. et al. Multi - dimensional meta - holography encrypted by orbital
598 angular momentum, frequency, and polarization. *Laser & Photonics Reviews*
599 **18**, 2301362 (2024).
- 600 26. Kim, J. et al. Geometric and physical configurations of meta - atoms for
601 advanced metasurface holography. *InfoMat* **3**, 739-754 (2021).

- 602 27. Park, C., Jeon, Y. & Rho, J. 36 - Channel spin and wavelength co -
603 multiplexed metasurface holography by phase - gradient inverse design.
604 *Advanced Science* **12**, 2504634 (2025).
- 605 28. So, S. et al. Multicolor and 3D holography generated by inverse - designed
606 single - cell metasurfaces. *Advanced Materials* **35**, 2208520 (2023).
- 607 29. Kim, J. et al. Metasurface holography reaching the highest efficiency limit
608 in the visible via one - step nanoparticle - embedded - resin printing. *Laser &*
609 *Photonics Reviews* **16**, 2200098 (2022).
- 610 30. Yu, Z. P. et al. Spin - orbit - locking vectorial metasurface holography.
611 *Advanced Materials* **37**, 2415142 (2025).
- 612 31. Qin, H. et al. Disorder-assisted real-momentum topological photonic
613 crystal. *Nature* **639**, 602-608 (2025).
- 614 32. Asad, A. et al. Wide - angled pragmatic dielectric chiral meta - platform for
615 spin - and wavelength - multiplexed holography in the ultraviolet and visible.
616 *Advanced Functional Materials* **34**, 2402744 (2024).
- 617 33. Gao, H. et al. Dynamic 3D meta-holography in visible range with large
618 frame number and high frame rate. *Science advances* **6**, eaba8595 (2020).
- 619 34. Park, C. et al. 12" Wafer-scale mass-manufactured metal-insulator-metal
620 reflective metaholograms by nanotransfer printing. *ACS Applied Materials &*
621 *Interfaces* **17**, 3749–3756 (2025).
- 622 35. Lee, C. et al. Inverse-designed metasurfaces for highly saturated
623 transmissive colors. *Journal of the Optical Society of America B* **41**, 151-158
624 (2024).
- 625 36. Jang, J. et al. Spectral modulation through the hybridization of

- 626 Mie-scatterers and quasi-guided mode resonances: realizing full and gradients
627 of structural color. *ACS Nano* **14**, 15317-15326 (2020).
- 628 37. Ren, R. Y. et al. Non-orthogonal polarization multiplexed metasurfaces for
629 tri-channel polychromatic image displays and information encryption.
630 *Nanophotonics* **10**, 2903-2914 (2021).
- 631 38. Wu, Y. K. et al. Dynamic structural colors based on all - dielectric Mie
632 resonators. *Advanced Optical Materials* **9**, 2002126 (2021).
- 633 39. Zang, X. F. et al. Polarization encoded color image embedded in a
634 dielectric metasurface. *Advanced Materials* **30**, 1707499 (2018).
- 635 40. Badloe, T. et al. Liquid crystal-powered Mie resonators for electrically
636 tunable photorealistic color gradients and dark blacks. *Light: Science &*
637 *Applications* **11**, 118 (2022).
- 638 41. Lim, K. T. P. et al. Holographic colour prints for enhanced optical security
639 by combined phase and amplitude control. *Nature Communications* **10**, 25
640 (2019).
- 641 42. Kim, I. et al. Pixelated bifunctional metasurface-driven dynamic vectorial
642 holographic color prints for photonic security platform. *Nature Communications*
643 **12**, 3614 (2021).
- 644 43. Yoon, G. et al. "Crypto-display" in dual-mode metasurfaces by
645 simultaneous control of phase and spectral responses. *ACS Nano* **12**,
646 6421-6428 (2018).
- 647 44. Wei, Q. S. et al. Simultaneous spectral and spatial modulation for color
648 printing and holography using all-dielectric metasurfaces. *Nano Letters* **19**,
649 8964-8971 (2019).

- 650 45. Bao, Y. J. et al. Full-colour nanoprint-hologram synchronous metasurface
651 with arbitrary hue-saturation-brightness control. *Light: Science & Applications*
652 **8**, 95 (2019).
- 653 46. Zhang, F. et al. Simultaneous full - color printing and holography enabled
654 by centimeter - scale plasmonic metasurfaces. *Advanced Science* **7**, 1903156
655 (2020).
- 656 47. Wen, D. D. et al. Multifunctional dielectric metasurfaces consisting of color
657 holograms encoded into color printed images. *Advanced Functional Materials*
658 **30**, 1906415 (2020).
- 659 48. Dai, Q. et al. A single - celled tri - functional metasurface enabled with
660 triple manipulations of light. *Advanced Functional Materials* **30**, 2003990
661 (2020).
- 662 49. Liang, C. L. et al. Single-celled multifunctional metasurfaces merging
663 structural-color nanoprinting and holography. *Optics Express* **29**, 10737-10748
664 (2021).
- 665 50. Khaleghi, S. S. M. et al. High resolution multicolor holograms encoded into
666 color print images with hybrid dielectric/plasmonic metasurfaces. *Applied*
667 *Physics Letters* **126**, 051102 (2025).
- 668 51. Yang, Y. et al. Revealing structural disorder in hydrogenated amorphous
669 silicon for a low - loss photonic platform at visible frequencies. *Advanced*
670 *Materials* **33**, 2005893 (2021).
- 671 52. Keawmuang, H. et al. Inverse design of colored daytime radiative coolers
672 using deep neural networks. *Solar Energy Materials and Solar Cells* **271**,
673 112848 (2024).

674